Ultramicroscopy 155 (2015) 62–73

Contents lists available at ScienceDirect

Ultramicroscopy

journal homepage: www.elsevier.com/locate/ultramic

The effect of pattern overlap on the accuracy of high resolution electron backscatter diffraction measurements

Vivian Tong [a,*], Jun Jiang [a], Angus J. Wilkinson [b], T. Ben Britton [a]

[a] Department of Materials, Imperial College London, Prince Consort Road, London SW7 2AZ, UK
[b] Department of Materials, University of Oxford, Parks Road, Oxford OX1 3PH, UK

ARTICLE INFO

Article history:
Received 26 January 2015
Received in revised form
24 April 2015
Accepted 26 April 2015
Available online 28 April 2015

Keywords:
Pattern overlap
Cross-correlation
Grain boundary
High-resolution EBSD

ABSTRACT

High resolution, cross-correlation-based, electron backscatter diffraction (EBSD) measures the variation of elastic strains and lattice rotations from a reference state. Regions near grain boundaries are often of interest but overlap of patterns from the two grains could reduce accuracy of the cross-correlation analysis. To explore this concern, patterns from the interior of two grains have been mixed to simulate the interaction volume crossing a grain boundary so that the effect on the accuracy of the cross correlation results can be tested. It was found that the accuracy of HR-EBSD strain measurements performed in a FEG-SEM on zirconium remains good until the incident beam is less than 18 nm from a grain boundary. A simulated microstructure was used to measure how often pattern overlap occurs at any given EBSD step size, and a simple relation was found linking the probability of overlap with step size.

1. Introduction

High resolution, cross-correlation-based electron backscatter diffraction (HR-EBSD) [1,2] determines relative elastic strains and rotations within a grain by measuring the pattern shifts between a reference EBSD pattern and test patterns (a review of the method can be found in Ref. [3]).

The potency and utility of HR-EBSD have been demonstrated in a variety of studies, such as mapping surface morphology of silicon at nanometre resolution [4], strain accommodation during martensitic transformation in steels [5] and Co-alloys [6,7], slip transfer at grain boundaries in Ti [8,9], deformation near nanoindents [10–12], stresses near inclusions in superalloys [13,14], type III stresses in deformed Cu polycrystals [3,15], stresses in Inconel-low alloy steel welds [16], in situ deformation of stainless steel [17], mapping stresses during in situ micropillar compression testing [18], SiGe/Si heterostructures [1,19,20], stress induced near edges of SiN layers on Si-on-insulator substrates [21], lattice strain and rotations in III–V nitride systems [22], c/a ratio variations in FeSeTe superconductors [23], residual strains near grain boundaries in Si [24], and elastic strains in 90° lamella domains in barium titanate [25]. In many of these studies there is interest in the stress variations close to grain boundaries or phase boundaries.

There have been various studies on the accuracy and sensitivity of strain and rotation measurements in HR-EBSD [26–28], the dependence of accuracy on the pattern centre position [20], and the effect of high frequency noise on strain sensitivity [2,26]. These studies are of experimental or simulated patterns all from grain interiors. Variations in strain and dislocation density near grain boundaries are often of interest [8,15,29], but the accuracy of HR-EBSD measurements near boundaries has not yet been quantified.

Approaching a grain boundary, the interaction volume samples two grains at once and results in a mixed diffraction pattern. Broadly, the intensity contribution from each grain is approximately proportional to the fraction of the interaction volume in that grain. This phenomenon has been used to measure the spatial resolution of the electron beam interaction volume [30] and the inclination angle of the grain boundary plane [31]. It is well known that measurement near grain boundaries may cause some uncertainty in EBSD measurements, as highlighted recently with conventional, Hough based, EBSD by Wright et al. [32].

For HR-EBSD, pattern mixing may result in increased uncertainty or even entirely erroneous pattern shift measurements. The degree of this uncertainty is not well known. Understanding and reducing the causes of this uncertainty is very important, as features such as stress concentrations and crack nucleation sites are often near grain boundaries. Fundamentally, uncertainty arises due to improper shift measurements, which are used to determine deviatoric strains and lattice misorientations between test and reference pattern [2].

Prior work has shown that the image cross-correlation method, when applied to unmixed patterns with limited noise, can measure sub-pixel shifts of ± 0.05 pixels with 256 pixel regions of interest (ROIs) dispersed within a $1\,k \times 1\,k$ image [26].

* Corresponding author.
E-mail address: v.tong13@imperial.ac.uk (V. Tong).

http://dx.doi.org/10.1016/j.ultramic.2015.04.019

This sensitivity decreases to around ± 0.2 pixels when artificial high frequency noise is added, but this can be partially compensated for if the low pass filter is adjusted to optimise the quality of the cross-correlation function, so that a sensitivity of ± 0.1 pixels can be achieved [2]. More recent studies have shown that optimising the capture settings can result in a sensitivity of ± 0.02 pixels [26,27].

In this study, the physical spatial resolution of HR-EBSD for this EBSD set-up is measured by determining the size of the interaction volume. This method measures the quality of cross-correlation on a line scan taken across a grain boundary, and has been used previously by Chen et al. [30].

One method of addressing potential noise due to pattern overlap so as to improve the effective spatial resolution, is to consider that Kikuchi bands contributed from the less dominant grain effectively act as low-frequency noise which can be filtered. If improperly filtered, this may result in a decrease in the cross-correlation peak height, as well as increased uncertainty in the cross-correlation function (XCF) peak position and hence error in the pixel shift measurements.

In practice, the exact distance of an EBSD point from the grain boundary can rarely be measured, and it is useful to know the statistical likelihood of pattern overlap. This has been measured for a given interaction volume size using a simulated microstructure. Voronoi tessellation is used to generate an exemplar microstructure. A grid of EBSD points at varying step sizes is overlaid on the microstructure. The fraction of points near a grain boundary which would exhibit any pattern overlap, or sufficient pattern overlap to cause significant error in the strain calculations (following the method outlined in [2]), is determined.

The effect of Fourier filtering on pattern overlap is addressed using a simple simulation to describe the overlapping volume of sampled material and the corresponding mixed diffraction pattern. Different filters are used to explore how filtering can reduce uncertainty and ideally improve accuracy of the technique. Filtering out low frequency components could attenuate features of the non-dominant pattern and improve cross-correlation measurements, increasing the effective resolution of HR-EBSD technique. A strategy for determination of optimum filter settings and errors is discussed.

2. Method

2.1. Sample preparation and pattern acquisition

Zircaloy-4 plate was cut and ground to 4000 grit finish, then polished in a 5:1 solution of colloidal silica and hydrogen peroxide for 4.5 h. This yielded a surface finish which showed grain contrast under polarised light. The sample was electropolished in a 9:1 solution of methanol and perchloric acid cooled with liquid nitrogen to -40 °C, at 30 V and 1 A/cm^2 for 60 s in order to produce high quality EBSD patterns.

Full resolution (1600×1152 pixels, 12 bit) diffraction patterns of Zircaloy-4 were captured from the interiors of distinct grains, on a Bruker eFlashHR detector mounted on in a Zeiss Auriga SEM. The SEM was operated at 20 keV and delivered a probe current of 10.5 nA measured using a Faraday cup, leading to an exposure time of 500 ms per pattern, for an intensity bit depth of 11.5 ($\sim$3000 grey levels). The EBSD pattern greyscale intensities were linearly mixed at different fractions to simulate the effect of pattern overlap near a grain boundary (Fig. 1).

2.2. Cross-correlation

Two hundred ROIs of size 256×256 pixels were extracted from the reference and each of the mixed diffraction patterns, and cross-correlated using in-house developed MATLAB scripts using a single pass of cross-correlation and the Wilkinson, Meaden and Dingley strain and rotation analysis method [2] with a robust iterative weighting scheme [33].

To isolate the effect of filtering, a known pixel translation was performed to shift the positions of features within test pattern away from the reference before mixing. This translation in the diffraction pattern corresponds, effectively, to a known small rotation and elastic strain between the new test and reference crystal, and enables accuracy of the cross-correlation function (XCF) peak determination to be measured. The translation was 2 pixels in X and 3 pixels in *Y* for the displacement gradient tensor calculations, and 20 pixels in both X and *Y* for the XCF peak shape calculations. If this translation is not imposed then ambiguity arises in interpreting any peak at the zero shift position in the XCF which could be generated by either a good registration of the diffraction information or by registration of undesired weaker contrast static background features when filtering has removed most of the diffraction contrast from the patterns. Fig. 2 shows the way in which the test and reference patterns were combined prior to cross-correlation analysis.

Band pass filters were applied in the Fourier domain to intensity normalised ROIs [2]. Band pass filters attenuate both high frequency noise (low pass component) and low frequency variation in the background (high pass component). The low pass component of the filter was set to 30 cycles/256 pixels, corresponding to the limits imposed by the detector optics [26]. Contributions at higher frequencies correspond to random noise and were removed by the filter. The high pass cut off frequency was varied between 0 (no filtering) and 14 cycles/256 pixels (severe filtering).

Fig. 3 shows an example ROI near a zone axis and the power spectrum of its Fourier transform as the high pass cut off frequency is increased. Increasing the high pass filter cut off attenuates low frequency components at the centre of the power spectrum. The back-transforms of the Fourier transforms show how features are progressively removed from ROI, with and without pattern overlap.

XCFs were computed for systematically selected combinations of filtering and mixing. The XCFs are normalised by the autocorrelation of the reference ROI, so an XCF peak height of 1 indicates perfect correlation. Displacement gradient tensors were calculated from measured X- and Y-shifts determined at each of the ROIs from the peak positions within their XCFs (using the Wilkinson, Meaden and Dingley (WMD) infinitesimal deformation framework [2] with iterative robust weighting route [33]).

Two error metrics are presented: actual error and mean angular error (MAE).

1. Actual error is the difference between applied and measured values. Here the displacement gradient tensor can be calculated directly from the imposed translation to give the actual solution. The difference from the direct calculation and the XCF measurement enables probing of the accuracy of the method.
2. MAE is calculated using the mean deviation from least squares fitting to the WMD analysis route. The MAE describes how well the shifts fit the WMD model, but may not reveal some systematic errors, which are captured by the actual error metric.

2.3. Spatial resolution of EBSD set-up

Spatial resolution in EBSD can be defined in two distinct ways.

(1) The *physical spatial resolution* is linked to the size of the

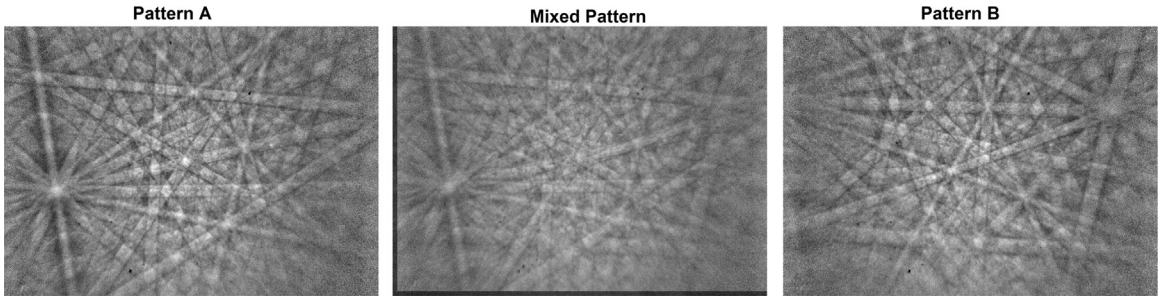

Fig. 1. Greyscale intensities in diffraction patterns A and B are translated and mixed to form mixed patterns.

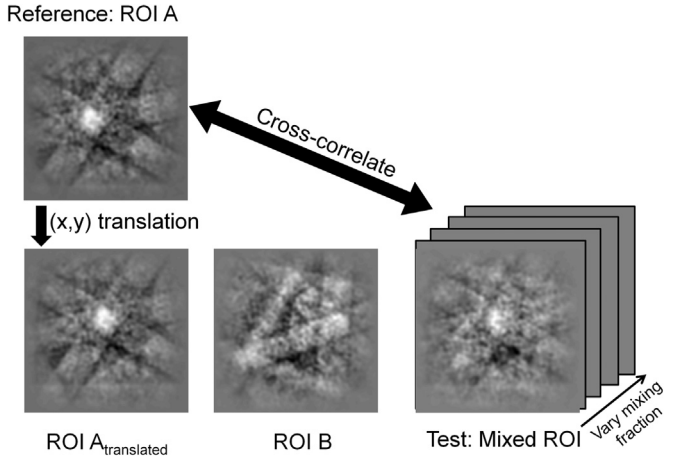

Fig. 2. ROI A is first translated, and then mixed with ROI B to different fractions. The mixed ROI are then correlated with ROI A.

interaction volume, from which the diffracted signal originates. Zaefferer defines it as the distance between an electron beam and a large-angle grain boundary, within which backscatter diffracted signal from both grain orientations can be obtained [34]. This is equivalent to the radius of the interaction volume if it is modelled as a hemisphere, as illustrated in Fig. 4(a).

In a typical EBSD set-up for a copper sample at incident beam energy of 20 keV and probe current of 10 nA, this is about 40 nm along the tilt axis, 120 nm perpendicular to the tilt axis, and 60 nm in depth [30]. The exact dimensions depend on accelerating voltage, probe current, and atomic number of the material.

(2) The *effective spatial resolution* [35] is based upon software algorithms used to discriminate one pattern from another. Here the limiting resolution is based upon where a mixed pattern cannot be indexed (in Hough-based EBSD), or cannot correlate well with the reference pattern to identify an image shift (in HR-EBSD). In practice, the effective spatial resolution is smaller than the physical spatial resolution, because it is possible to separate signal of one grain from another if one pattern has much higher intensity than the other pattern [35].

The physical spatial resolution, or interaction volume size, was measured using a cross-correlation method based upon the work by Chen et al. [30]. Fig. 4(b) shows that a line scan of 20 patterns across a grain boundary was taken in 20 nm steps aligned at 40° to the grain boundary, in order to avoid carbon contamination on the sample, which degrades pattern quality. This resulted in an effective step size of 15 nm normal to the grain boundary. The sample was aligned so that the trace of the grain boundary on the sample surface was normal to the tilt axis but the alignment below the surface was unknown. As the grain boundary is aligned 40° from the microscope tilt axis, the measured interaction volume radius lies between the spatial resolution parallel and perpendicular to the tilt axis. The resolution parallel to the tilt axis is up to three times smaller than perpendicular to it, so this measurement is moderately conservative compared with other studies.

Each pattern in the line scan was cross-correlated against the two extreme patterns and peak heights of the XCFs plotted. The peak heights were normalised to range between 1 and 0 and the values multiplied then normalised, producing a peak with a full width at half maximum (FWHM) of 59 nm. Fig. 4(c) shows the normalised XCF peak heights of the line scan (red and black lines) and the normalised peak obtained from multiplying these values (blue line). The XCF peak height profile is relatively symmetric suggesting that the boundary plane was fairly close to normal to the sample surface.

A model of a hemispherical interaction volume crossing a grain boundary was used to relate the FWHM to the interaction volume radius. Volume fraction of the hemisphere in the reference grain was plotted as a function of perpendicular distance from the grain boundary. This produced Fig. 4(d), a plot similar to the peak heights in Fig. 4(c).

Fig. 4(d) shows that the FWHM should be approximately equal to the interaction volume radius. The FWHM in the simulation was measured as 61 nm, approximately equal to the 59 nm interaction volume radius. This is different to the interpretation described in Chen et al., where the FWHM is described as twice the interaction volume radius. Since the FWHM measured in the EBSD line scan in Fig. 4(c) is 59 nm, our model indicates that the interaction volume is also approximated as a 59 nm radius hemisphere.

2.4. Pattern mixing to mimic overlap near grain boundaries

The interaction volume was modelled as a 59 nm radius hemisphere, corresponding to the interaction volume of this EBSD set-up. The grain boundary is assumed to run perpendicular to both the free surface and the scan line. The distance from the centre of the interaction volume to the grain boundary was calculated for different mixing fractions, assuming that the intensity fraction is directly proportional to the volume fraction of the contributing grain within the assumed hemispherical interaction volume. This is a simplified model of the interaction volume which provides an indicative link between the proportions of mixed pattern intensity with a physical distance from the grain boundary; it is only meant as an approximate guide and would clearly vary with beam conditions and sample type. Fig. 5 illustrates the non-linear weighting of pattern mixing with distance from the grain boundary.

11 linearly spaced mixing fractions were used, corresponding to distances between the incident beam position and the grain boundary given in Table 1.

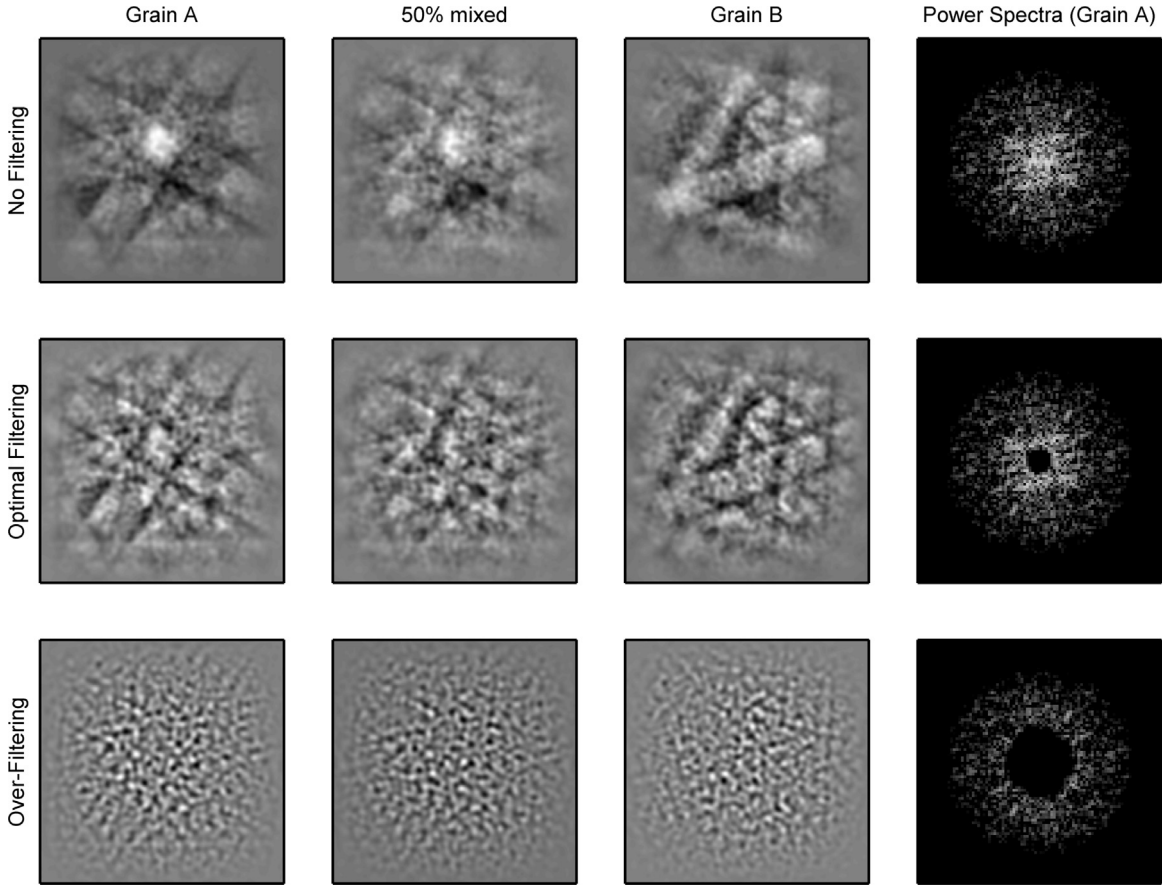

Fig. 3. Effect of the high pass filter and pattern mixing on ROIs and power spectra. Optimal filtering: High pass cut off = 5.4 cycles/256 pixels. Over-filtering: High pass cut off = 14 cycles/256 pixels.

3. Results

3.1. Effect of pattern overlap on the cross-correlation function (XCF)

3.1.1. Effects of high pass filter on XCF peak

Fig. 6 shows the effect of filtering on the XCF peak shape for 50:50 mixed patterns. When no high pass filter is applied, the correct peak (indicated by red arrows) is broad and peak position is poorly defined. The peaks become rounder and sharper as filtering increases. Large high pass filter cut off frequencies cause a secondary peak to appear at (0,0) displacement (as indicated by the white arrow), and the correct XCF peak is very narrow, which makes upsampling for sub-pixel interpolation difficult.

3.1.1.1. Onset of zero peak. The onset of the secondary peak at (0,0) displacement is shown in the XCF peak profile in Fig. 7(a) to begin to form as the high pass filter cut off frequency is increased to 5.6 cycles/256 pixels with pattern mixing at 70% reference intensity (16 nm from the grain boundary). This peak is not present at lower high pass cut offs (blue dashed line) and is very pronounced at large high pass cut offs (brown dashed line). The shape of the correct global XCF peak at (20,20) displacement is shown in Fig. 7(b) for comparison.

3.1.2. Effect of distance from grain boundary on XCF peak

Fig. 8 shows how the XCF varies as the pattern mixing is altered to simulate approaching a grain boundary with high pass filter of 5.4 cycles/256 pixels. The XCF shows a clear peak (but a lower peak height) at mixing down to 40% reference intensity, when the centre of the interaction volume is on the other side of the grain boundary (shown as negative distances). At 20% reference intensity, or 25 nm on the other side of the grain boundary, other peaks begin to form, indicating poor correlation with the reference pattern.

3.1.3. Error in measured XCF shifts

Actual error in the XCF shifts is given by the length of the difference between the measured translation vector, $\boldsymbol{Q}^{\text{measured}}$, and the imposed translation $\boldsymbol{Q}^{\text{imposed}}$.

$$\text{Actual error} = \sqrt{\left(Q_1^{\text{measured}} - Q_1^{\text{imposed}}\right)^2 + \left(Q_2^{\text{measured}} - Q_2^{\text{imposed}}\right)^2} \quad (1)$$

With the reference intensity at 70% the actual error in the XCF shifts has a minimum of 0.305 pixels at a filter high pass cut off between 5.4 and 5.8 cycles/256 pixels (Fig. 9, blue line).

The mean angular error (MAE) in the XCF shifts decreases with increasing high pass cut off and does not show a minimum (Fig. 9, green line).

3.2. Effect of pattern overlap on displacement gradient tensor

3.2.1. Variation with pattern mixing fraction

In Figs. 10 and 11, only the displacement gradient tensor components A_{13} (red circles) and A_{23} (green squares) should have non-zero values.

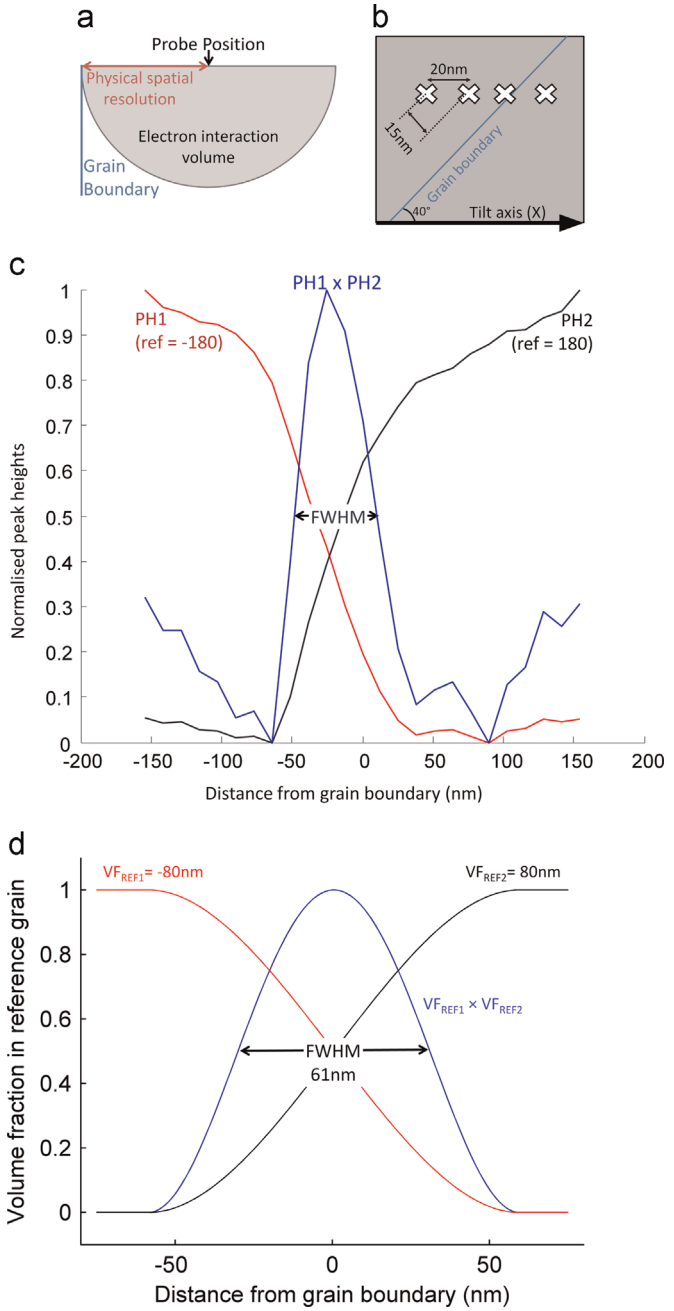

Fig. 4. (a) Physical spatial resolution in EBSD (after Zaefferer [34]). (b) Microscope set-up of grain boundary line scan. (c) Peak heights from XCFs of a line scan multiplied to calculate size of interaction volume. (d) Simulated line scan to relate the interaction volume radius to the measured FWHM. (For interpretation of the references to colour in this figure, the reader is referred to the web version of this article.)

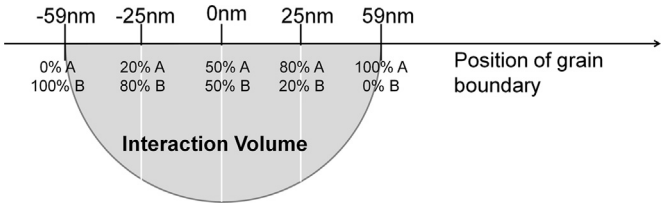

Fig. 5. Different mixing fractions correspond to different positions of the grain boundary intersecting the interaction volume.

Table 1
Mixing fraction, or reference intensity, modelled as the distance from the grain boundary in a hemispherical interaction volume (shown in Fig. 5).

Reference intensity (%)	100	90	80	70	60	50	40	30	20	10	0
Dist. from g.b. (nm)	59	36	25	16	8	0	−8	−16	−25	−36	−59

$$Q_1 = r_2A_{12} + r_3\boldsymbol{A_{13}} - \frac{r_1^2}{r_3}A_{31} - \frac{r_2r_1}{r_3}A_{32} + r_1(A_{11} - A_{33})$$
$$Q_2 = r_1A_{21} + r_3\boldsymbol{A_{23}} + - \frac{r_2r_1}{r_3}A_{31} - \frac{r_2^2}{r_3}A_{32} + r_2(A_{22} - A_{33}) \quad (2)$$

This arises from the imposed (Q_1,Q_2) pattern shift to one of the diffraction patterns, which is used to determine accuracy of measurements. The values of Q_1 and Q_2 are consistent for all the ROI. Any of the terms with an r_1 or r_2 component (which change depending on ROI position) must therefore go to zero. This leaves only A_{13} and A_{23} (terms marked in bold in Eq. (2)) that vary with Q_1,Q_2, and these are only dependent on the detector distance r_3.

For an imposed pixel shift of $(Q_1, Q_2) = (2, 3)$ with a pattern centre of $X^* = 0.46$, $Y^* = 0.57$, $Z^* = 0.53$ (where Z^* is measured as a fraction of detector X-axis), the displacement gradient tensor components are $A_{13} = 0.0024$ and $A_{13} = 0.0035$.

In Fig. 10, the accuracy of the displacement gradient tensor decreases as the interaction volume approaches and crosses a grain boundary. For optimally filtered patterns, the deviation at 70% reference intensity, or 16 nm from the grain boundary, is less than 5×10^{-4}.

3.2.2. *Variation with high pass filter cut off frequency*

Fig. 11 shows the variation of the displacement gradient tensor at 70% reference intensity (16 nm from the grain boundary). The two non-zero components A_{13} and A_{23} remain fairly constant despite large changes in the high pass filter cut off frequency. The systematic error from the actual solution in the non-zero A_{13} and A_{23} components comes from correlating a mixed pattern, which is shown in Fig. 10 to increase with increasing mixing fraction.

All other components, which have an actual solution of zero, converge towards zero at large high pass cut off frequencies.

3.2.2.1. Error in the displacement gradient tensor variation with high pass filter. Actual error in the displacement gradient tensor is given by magnitude of the difference between the measured displacement gradients, A^{measured}, and the displacement gradients caused by the imposed pixel shift A^{imposed}.

$$\text{Actual error} = \left|A^{\text{measured}} - A^{\text{imposed}}\right| \quad (3)$$

Fig. 12(a) shows that for components of the displacement gradient tensor with an actual solution of zero, over-filtering generally decreases the measurement error. For components A_{13} (red circles) and A_{23} (green squares), which have a non-zero actual solution, the error is minimum at a high pass cut off between 4 (A_{23}) and 8 (A_{13}). This is the optimum filter set-up.

As seen in Fig. 12(b), for all components the error in the displacement gradient tensor is below 3×10^{-4} at optimal filtering. For all components except A_{11} and A_{31}, appropriate filtering increases the accuracy of the displacement gradient tensor measurements, though the gains are sometimes rather modest.

3.2.2.2. Random error from ROI positioning. Even when using 200 ROIs, error in the displacement gradient tensor components can vary by up to 1.5×10^{-5} depending on where the ROI are placed (this problem is seeded always with 1 ROI in the centre, 19 in a

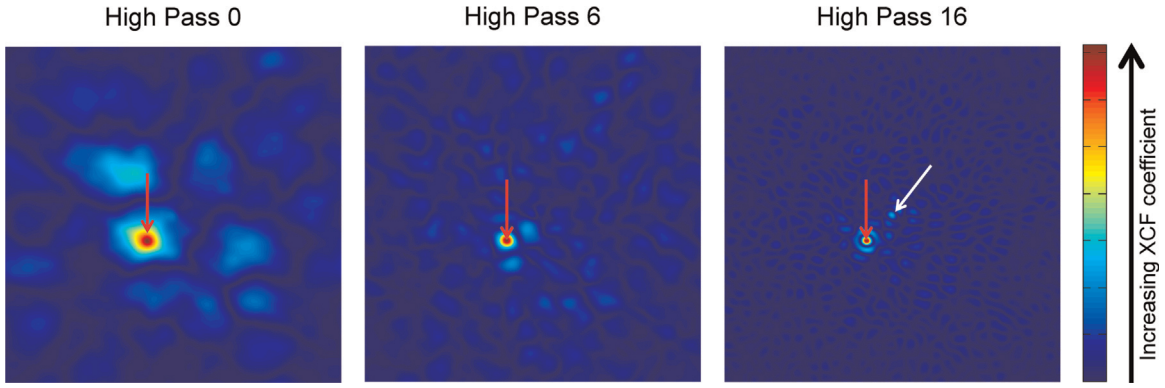

Fig. 6. Effect of filtering on the XCF, 50% reference intensity, modelled as directly on the grain boundary. The white arrow indicates the peak at (0,0), and the red arrow the desired peak at (20,20).

ring in the diffraction pattern, and the rest using the random number generator in MATLAB). Fig. 13 shows the spread in error of the non-zero displacement gradient tensor components A_{13} and A_{23}, after five separate measurements. The minima in error are between 4 and 5 for A_{13} and between 7 and 8 for A_{23}, consistent with the minima in error shown in Fig. 12(a).

3.3. Generalisation to many grain boundaries

The previous figures have been a detailed analysis of one particular grain boundary. The following section repeats the same analysis for different grain boundaries, simulated by mixing patterns from different grain interiors. The error metric used is the actual shift error as defined in Eq. (1), and this is plotted as the blue line ('Actual error') in Fig. 9.

Cross-correlation was performed on 210 simulated grain boundaries, and pattern shift errors obtained from the imposed and measured pattern translations. The mean pixel shift accuracy as the interaction volume approaches a grain boundary is given in Fig. 14 for unfiltered patterns. The dashed lines (labelled $0.1\varepsilon_y$ and 18 nm) show the threshold for significant strain error in HR-EBSD measurements, or one tenth of the yield strain for most metals ($\varepsilon_y = 2 \times 10^{-3}$, so $0.1\ \varepsilon_y = 2 \times 10^{-4}$).

Fig. 14 shows that the pixel shift error is small (0.03 pixels) when there is no pattern overlap and increases to 0.75 pixels at the grain boundary (50% reference intensity). The strain error can be linked to pixel error by Eq. (4), from Britton et al. [26]:

$$\text{Strain error} = \frac{m \times \text{Pixel error}}{\text{Image width}} \tag{4}$$

The resolution figure of merit m ranges between 0.4 and 1 depending on camera geometry, and a smaller value indicates better accuracy. Since m was not measured directly in this case, a conservative estimate of 1 was used and the image width here was 1600 pixels. Using these values, Eq. (4) has been used to generate the second *Y* axis displaying strain error in Fig. 14.

Histograms of the distributions of shift errors at 59 nm (no mixing) and 16 nm (70% reference intensity) from the grain boundary are shown in Fig. 15.

Fig. 15(a) shows the noise floor of HR-EBSD, obtained by correlating unmixed patterns. The mean value is 0.0313 pixels. Fig. 15 (b) shows the distribution of errors with high pass cut offs of 0, 5.4 and 12 cycles/256 pixels, corresponding to no filter, optimal filtered, and over filtered patterns respectively.

The histogram in Fig. 15(b) shows that accuracy at 70% reference intensity, or 16 nm from the boundary, is similar between unfiltered and optimal filtered patterns (any difference is around the noise floor of HR-EBSD, shown in Fig. 15(a)). Over-filtering patterns significantly increases error.

3.4. Statistical likelihood of overlap

Now that the error associated with pattern overlap has been measured in Fig. 14, it is important to consider how often pattern overlap occurs, and the degree of overlap when it occurs.

Fig. 16(a) shows a test microstructure of 50 grains in a 500 μm by 500 μm box constructed using Voronoi tessellation and seeded with the random number generator in MATLAB, producing a microstructure with an average grain size of 10 μm.

Grids of points at step sizes of 10, 8, 6, 4, 2, 1, 0.5, 0.2, 0.1, and 0.05 μm were overlaid on the microstructure and the Euclidean distances from each point to the nearest grain boundary calculated. If we consider only those points in the map that are within one step of a grain boundary we can then determine the fraction of grain boundary points that are within a threshold distance, sufficiently close for various extents of pattern overlap to occur. When the step size is less than the chosen threshold distance from the grain boundary, then the region within 1 step of the boundary will always contain at least 1 point within the threshold distance.

Given the simple model of the interaction volume the pattern overlap begins when the incident beam is at 59 nm from the grain boundary and the upper blue line in Fig. 16(b) shows the likelihood of grain boundary points showing any degree of pattern overlap. Fig. 14 shows that strain errors of 2×10^{-4} are generated by pattern overlap when the incident beam is 18 nm from the boundary. The lower red line in Fig. 16(b) shows the fraction of grain boundary points expected to fall within 18 nm of the boundary and thus have sufficient pattern overlap to cause significant strain error. These fractions were found to follow the relation in Eq. (5).

Each grid was displaced from itself ten times and the fraction of points within the threshold distances of 18 nm and 59 nm counted. This produced a spread in the results. Average values are plotted as circles in Fig. 16(b) and error bars represent 1 standard deviation in the distribution.

$$\text{Likelihood}\ (d < x) = \frac{x}{\text{step size}} \tag{5}$$

x = threshold distance, d = distance from boundary.

For a 0.2 μm step size, 30% of points that are already within 1 step of the grain boundary will have some pattern overlap, but only 9% of points will have significant strain error associated with the pattern overlap. This percentage varies with the step size according to Eq. (5).

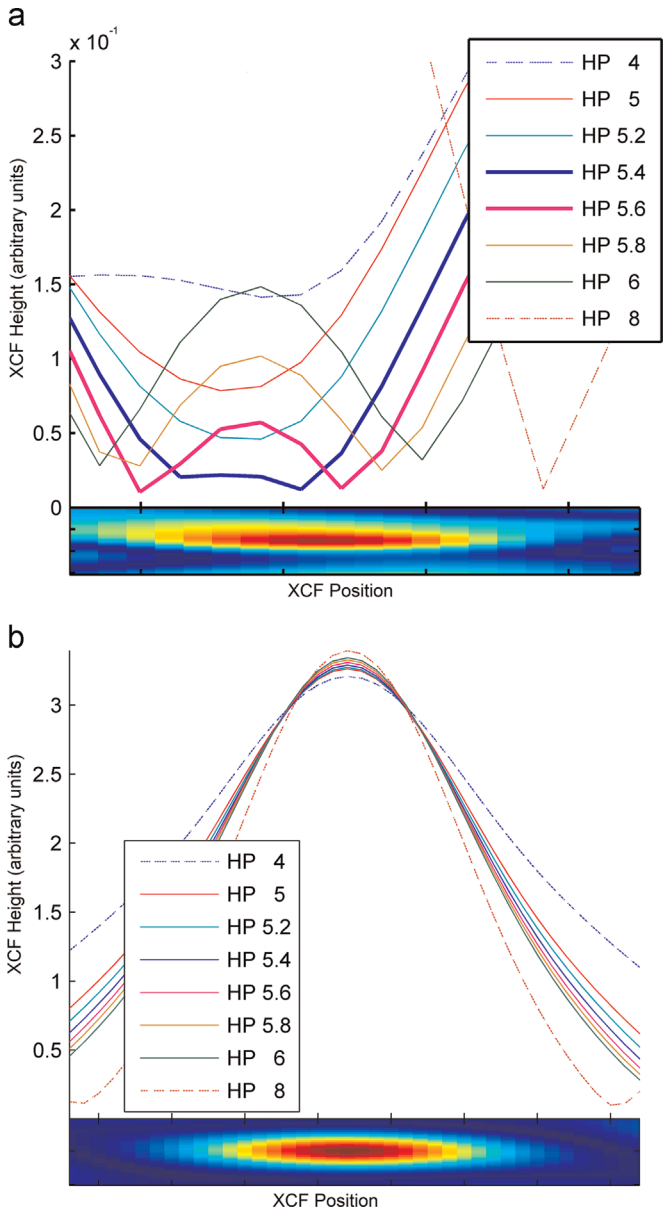

Fig. 7. (a) Line profiles of the secondary peak at (0,0) displacement, 70% reference intensity, where the second peak begins to form at high pass cut off of 5.6 cycles/256 pixels (pink line). X-axis given as 2D profile of the peak centre showing the position of the second peak when high pass cut off is 14 cycles/256 pixels. (b) line profiles of the global XCF peak, with 70% reference intensity. X-axis given as 2D profile of the XCF peak showing peak position at a high pass cut off of 14 cycles/256 pixels. The legend boxes indicate the high pass cut off frequencies used in the line profiles. (For interpretation of the references to colour in this figure legend, the reader is referred to the web version of this article.)

4. Discussion

Two diffraction patterns from grain interiors were mixed at different ratios to simulate pattern overlap, and cross-correlation was performed on the mixed patterns using the unmixed pattern as reference. The results show that a zero pattern shift peak develops in the XCF at large high pass cut off frequencies and the onset of this was used to determine an optimal filter. Pixel shift and strain accuracy of HR-EBSD were measured as a function of reference pattern intensity which was connected through a simple and approximate model to the distance of the incident beam from the grain boundary.

4.1. Effect of filtering

To optimise measurement of image shifts using cross correlation (i.e. for elastic strain measurement) typical upsampling methods require sufficient information within the peak to identify the 'best' shift with sub-pixel interpolation. This drives towards an optimal peak shape that is round and not too sharp. Fig. 6 shows that the ideal peak shapes can be formed with appropriate high pass filtering, with cut off frequencies between 4 and 8 cycles/256 pixels. Less filtering results in blurry peaks and over-filtering results in very sharp peaks and both of these situations are not ideal for interpolation of the exact peak position.

It can be difficult to determine the best filtering conditions, as in practise high-precision can be obtained through over-filtering where all useful information in the pattern is removed such that a prominent zero peak appears (Fig. 6) and the mean angular error reduces (Fig. 9) toward zero.

Fig. 9 shows that accuracy is limited by over-filtering, even though precision improves at large filter cut offs. Therefore choosing an appropriate filtering condition to ensure accuracy, when the absolute strain between two patterns is unknown, can be explored using pattern translation. Here the optimal filter cut off is determined to be just before the onset of the zero peak in Fig. 7, at 5.4 cycles/256 pixels.

4.2. Effect of mixing

Fig. 10 shows that even for an optimal filter, accuracy is limited when the mixing fraction increases to less than 70% of the reference pattern, modelled here as 16 nm from the grain boundary.

In practice, the presence of a clear XCF peak shape in Fig. 8 does not necessarily mean that the correct XCF has been identified. Near grain boundaries, the XCF should be computed for both potential reference grains and the XCF with the higher peak height preferred. Care should be taken to use the same filter setting, since increasing the high pass cut off increases the peak height.

4.3. Errors

Only the non-zero components of the displacement gradient tensor have been used to determine the optimal filter (bold lines in Fig. 12(a)). It is not helpful to include the zero components of the displacement gradient tensor in treatment of errors, since they generally tend towards zero when the ROI is over-filtered (Fig. 11). These measurements tend towards the correct solution due to the false zero peak, even though accuracy of the XCF shift measurement at large high pass cut offs is worse.

The minima in error of displacement gradient components A_{13} and A_{23} are at high pass cut offs of around 8 and 4 cycles/256 pixels respectively. This confirms that an optimal filter cut off of $\sim$5.4 is appropriate, since it is in between these two values.

Mean angular error (MAE) measures the internal consistency and not the accuracy of the displacement gradient solution. In the case of mixed patterns, Fig. 9 shows that over-filtering decreases the accuracy, but increases the consistency but only because the pattern shifts are drawn towards the false zero displacement peaks and hence towards a displacement gradient tensor with a smaller norm. Therefore, MAE is a not a good error metric to determine the best filter settings (note that it is still indicative of whether the shifts relate to a consistent deformation gradient between the two patterns and is therefore useful).

Random errors in the displacement gradient tensor (Fig. 13) are small ($< 1.5 \times 10^{-5}$), and decrease with increasing filtering to large high pass cut offs. In this case, they do not affect the choice of optimal filter (position of the minima in displacement gradient tensor components) and therefore multiple measurements are not

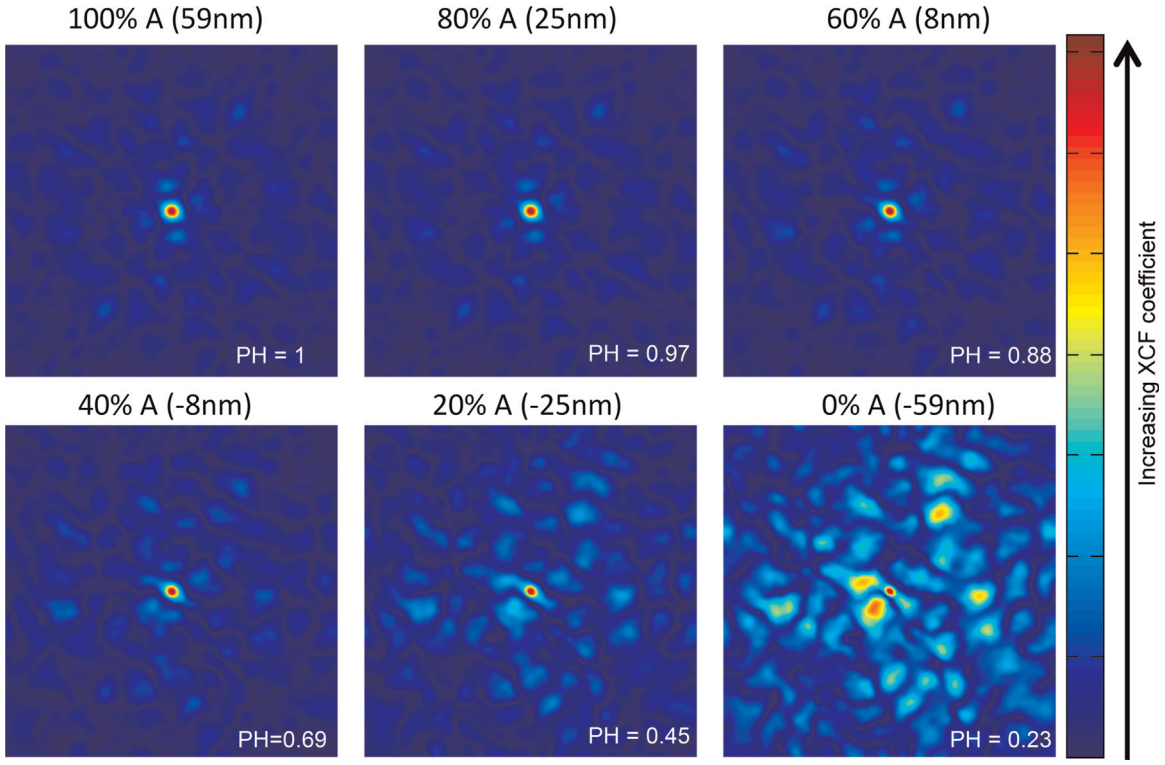

Fig. 8. XCF as the interaction volume approaches and crosses a grain boundary with a high pass cut off of 5.4 cycles/256 pixels (optimal filter setting). PH=normalised XCF peak height.

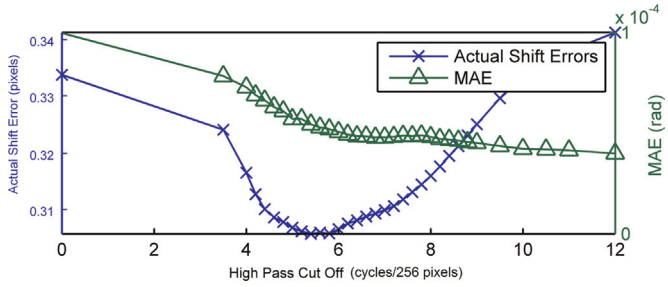

Fig. 9. Actual error and MAE in the XCF pixel shifts, 70% reference intensity modelled as 16 nm from grain boundary. (For interpretation of the references to colour in this figure, the reader is referred to the web version of this article.)

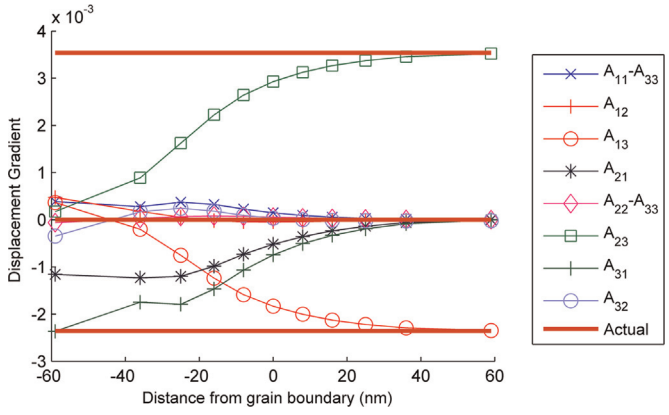

Fig. 10. The displacement gradient tensor as a function of mixing fraction, modelled as distance from the grain boundary, for optimal high pass cut off=5.4 cycles/256 pixels, with inclusion of the expected (Actual) displacement gradient values from the pattern translation – $A_{13}=3.5\times10^{-3}$, $A_{23}=-2.4\times10^{-3}$, all other components of $A=0$. (For interpretation of the references to colour in this figure, the reader is referred to the web version of this article.)

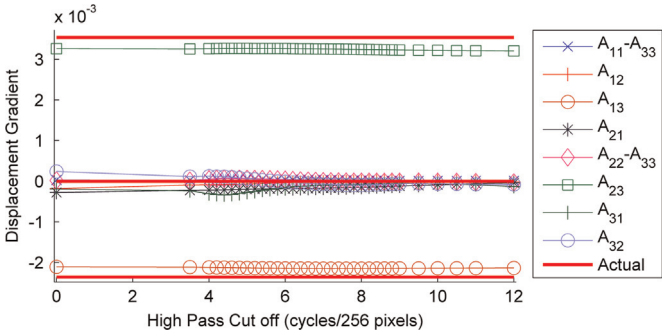

Fig. 11. The displacement gradient tensor for a reference pattern correlated with a translated 70% reference pattern (i.e. 16 nm from grain boundary) with varying high pass cut off filtering. The actual values are determined from the imposed pattern translation. (For interpretation of the references to colour in this figure, the reader is referred to the web version of this article.)

needed to determine the optimal filter.

4.4. Likelihood of overlap in a typical HR-EBSD scan

Although Fig. 9 shows that the accuracy in XCF shift is in some cases improved by filtering, Fig. 15(b) shows that this is not generally true. The accuracy can be improved in some patterns, as shown by the minima in the actual error in Fig. 9. Therefore, high pass filters should not be used in HR-EBSD if the patterns are already background corrected. In the case where patterns are not background corrected, a high pass filter can be used to remove the background.

Fig. 14 shows that strain error caused by pattern overlap 18 nm from the boundary is 2×10^{-4}, and increases as the interaction volume approaches the grain boundary. The noise level for EBSD strain measurements within the grain interior varies somewhat with pattern acquisition settings but is typically at the $\sim10^{-4}$

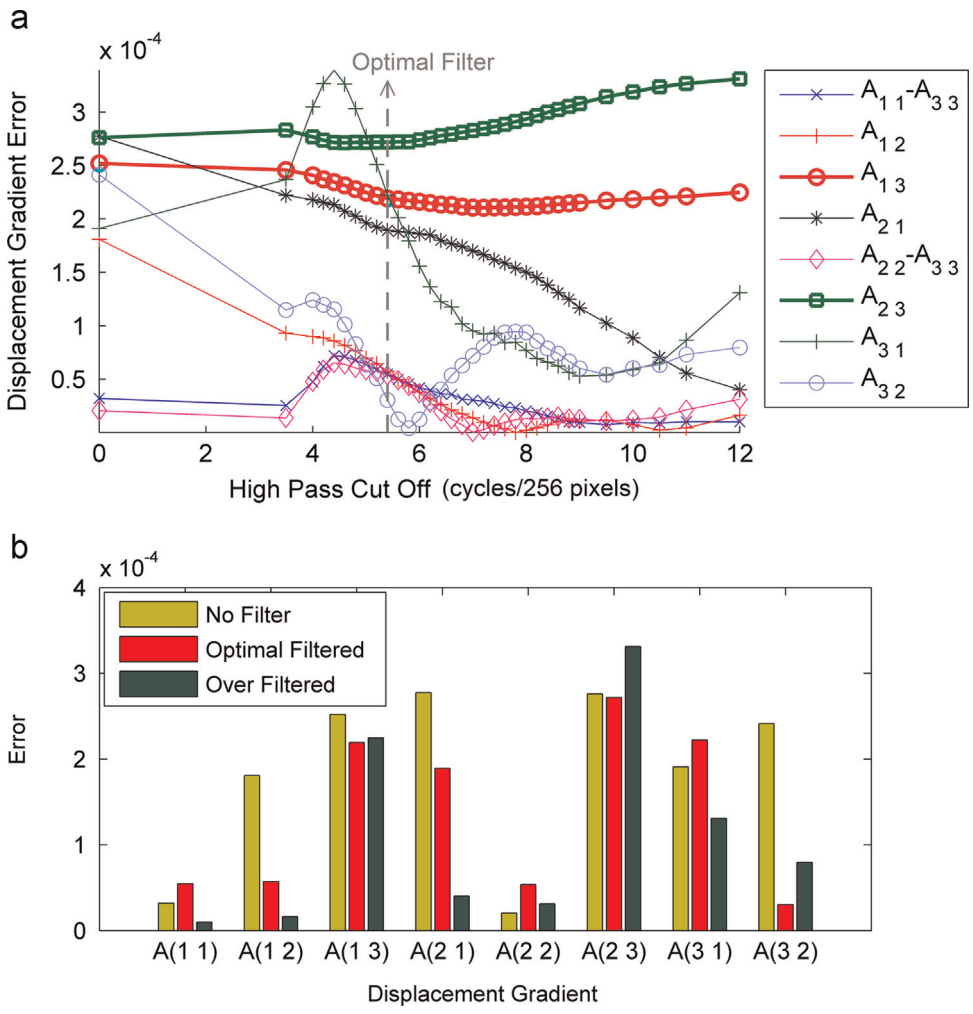

Fig. 12. Magnitude of error in each component of the displacement gradient tensor for different filters. Non-zero components are A_{13} (red circles) and A_{23} (green squares), marked in bold. Bottom: bar chart of error in the displacement gradient tensor components for no filtering, optimal filtering, and over-filtering. 70% reference intensity modelled as 16 nm from grain boundary. (For interpretation of the references to colour in this figure legend, the reader is referred to the web version of this article.)

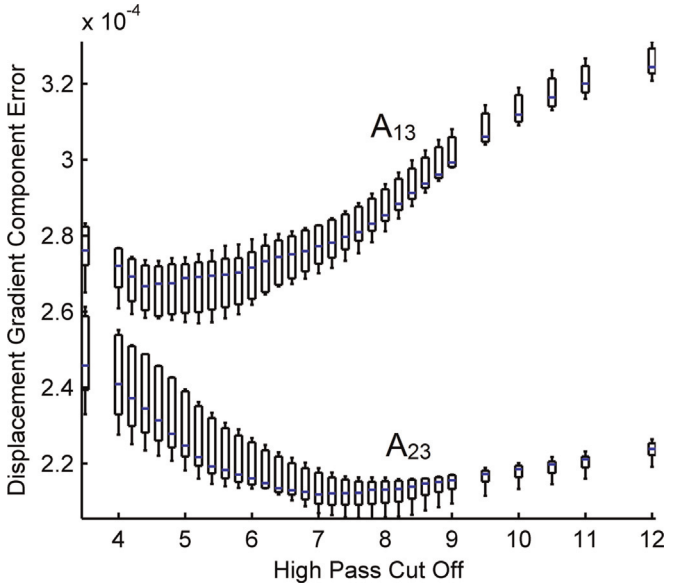

Fig. 13. Box and whisker plot showing the variation in displacement gradient error varying with ROI location (the box shows the mean, 75% and 25% range; the whiskers show the total range).

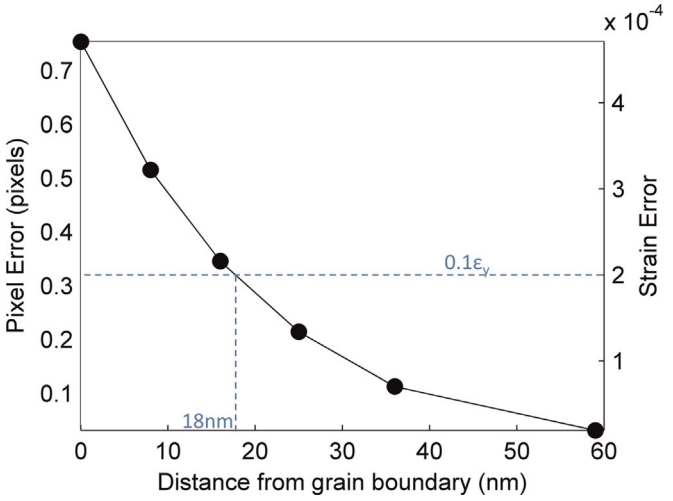

Fig. 14. Average pixel shift and strain errors as the interaction volume approaches a grain boundary (unfiltered patterns).

level. Thus it is only when the incident beam is closer than 18 nm to the grain boundary that pattern overlap may appreciably affect errors in the measurement. The yield strain for most metals is

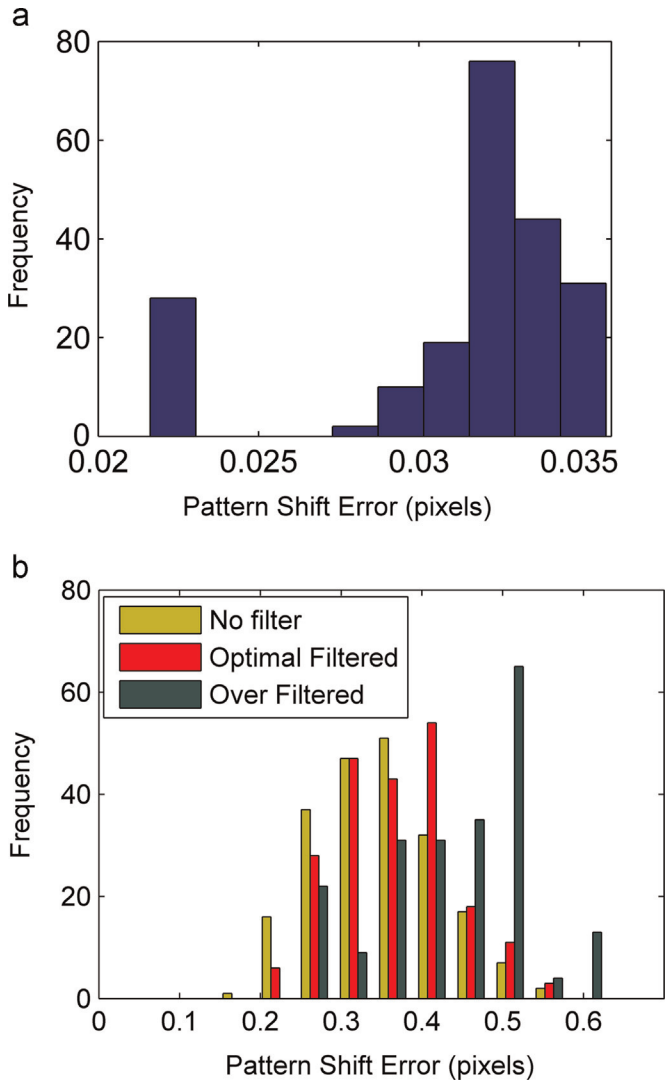

Fig. 15. (a): Histogram of pattern shift errors for patterns with no overlap – noise floor of HR-EBSD technique. (b): Histogram of pattern shift errors for 70% reference mixed patterns (16 nm from grain boundary) for different filters. (For interpretation of the references to colour in this figure, the reader is referred to the web version of this article.)

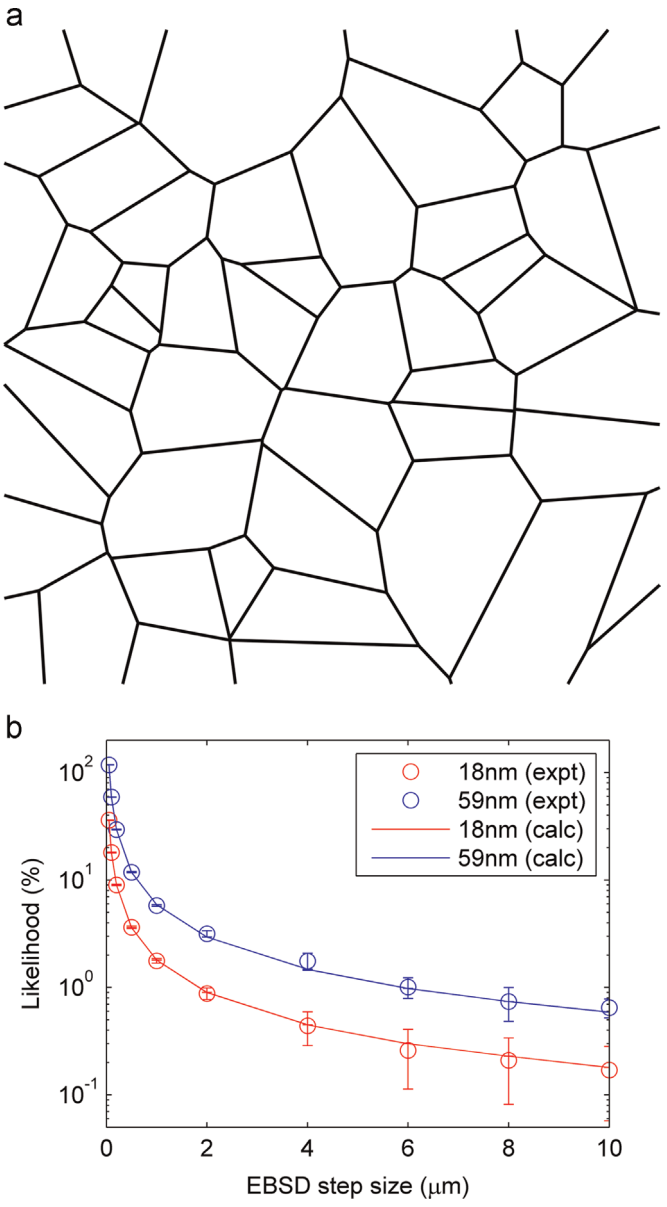

Fig. 16. (a): Test microstructure used to calculate the fraction of points near a grain boundary with pattern overlap. (b): Probability of a point near a grain boundary with pattern overlap (blue) or significant strain error (red). (For interpretation of the references to colour in this figure legend, the reader is referred to the web version of this article.)

2×10^{-3}, one order of magnitude higher. Therefore, elastic strains can be measured accurately up to 18 nm from the grain boundary.

The physical conversion of the intensity ratio in the overlapped region corresponds to 18 nm in this material (Zircaloy-4) and the microscope settings used here. In this case, the volume has been conservatively approximated: the beam has been scanned at an incident angle to the grain boundary and a simple hemisphere model has been used to extract the equivalent interaction volume radius. The backscattered interaction volume radius decreases with increasing atomic number. The equivalent extent of pattern mixing (72% reference intensity) is general and can be calculated for each material, using the pattern intensity mixing approach shown in Section 3.4.

In practice the quality of diffraction patterns may locally decrease due to increase in microstructural hetereogenity towards the grain boundary interface especially in plastically deformed samples. This breaks the local symmetry of the crystal and blurs the diffraction bands, thus reducing the quality of the cross correlation process. Typical HR-EBSD studies include a normalised peak height measurement which can be used as a direct thresholding tool. In cases where accurate measurement of the strain and rotation gradients for particular grain boundaries is important, the effect of pattern overlap alone can be understood through simple mixing experiments as proposed here and as pattern simulation tools improve (taking into account full intensity distributions, optical noise from the capture system, as well as defect populations) it is likely that confidence in these measurements will continue to improve.

Since the distance of a point from the grain boundary cannot be measured directly from the discrete sampling of an EBSD scan, points with large strain error cannot be identified. Therefore, the fraction of points < 18 nm from a boundary should ideally be as low as possible. Fig. 16(b) shows that in an EBSD scan with a small step size of 0.2 μm, only 9% of points within one step of a grain boundary are also within 18 nm from the boundary, and therefore exhibit pattern overlap leading to significant strain error, and this percentage decreases with increasing step size.

There have been several studies using cross-correlation-based EBSD to measure stresses and lattice rotation near grain boundaries. Hotspots in geometrically necessary dislocation density distributions have been shown to occur near grain boundaries after plastic deformation of Cu [15,36] and Ti–6Al–4V polycrystals [37]. Similarly a propensity for higher residual stresses near grain boundaries in deformed Cu has been observed [38], and more detailed analysis have been made of local stress intensities near grain boundaries that block slip bands in Ti [8,9]. In each of these cases the step size was relatively large compared to the expected interaction volume dimensions and the local stress features typically persisted beyond just the nearest pixels to the grain boundaries. The work reported here confirms that pattern overlap does not significantly alter any of the results or conclusions drawn in these works. Very recent work by Nacke et al. [24] has reported very fine scan step (5 nm) measurements of lattice strains measured close to different boundary types in Si. The measurements they made at 10 kV and 10 nA and a region extending 50 nm on either side of the boundary exhibited pattern overlap and so was excluded in their presented results. Our analysis suggests that data could have been included from regions somewhat closer to these boundaries despite the pattern overlap.

5. Conclusions

(1) High pass filtering can have an effect on the XCF shape and generate false zero peaks when over-filtered.
(2) Pattern overlap affects elastic strain measurement accuracy within 18 nm of the grain boundary for this EBSD set-up (Zircaloy-4 sample, 20 kV, 10.5 nA beam, Zeiss Auriga FEG-SEM with Bruker eFlash EBSD camera). It is likely that this will vary with material (atomic number, local boundary structure), and microscope settings (emitter type, voltage, probe current, and exposure time).
(3) Peak height and mean angular error are measures of precision but not accuracy. This work outlines how to determine the accuracy of HR-EBSD near a grain boundary using simple calibration tests.
(4) The high pass filter can sometimes improve accuracy but this is not generally true for background corrected EBSD patterns.
(5) Statistically speaking pattern overlap is unlikely to create significant artefacts in HR-EBSD measurements at grain boundaries, even at relatively small (0.2 μm) step size. The use of HR-EBSD to measure residual elastic strains and GND density near boundaries has therefore been validated.

Acknowledgments

The authors would like to thank Drs Stuart Wright, Eleanor Clarke, Phani Karamched and Philip Littlewood for helpful discussions over the years concerning pattern overlap at grain boundaries and its effects on HR-EBSD measurements. Funding contributions are acknowledged from ESPRC through the HexMat Grant (EP/K034332/1), Rolls-Royce plc and AVIC-BIAM.

References

[1] A.J. Wilkinson, G. Meaden, D.J. Dingley, High resolution mapping of strains and rotations using electron backscatter diffraction, Mater. Sci. Technol. 22 (2006) 1271–1278.
[2] A.J. Wilkinson, G. Meaden, D.J. Dingley, High-resolution elastic strain measurement from electron backscatter diffraction patterns: new levels of sensitivity, Ultramicroscopy 106 (2006) 307–313.
[3] T.B. Britton, J. Jiang, P.S. Karamched, A.J. Wilkinson, Probing deformation and revealing microstructural mechanisms with cross-correlation-based, high-resolution electron backscatter diffraction, J. Manag. 65 (2013) 1245–1253.
[4] M.D. Vaudin, G. Stan, Y.B. Gerbig, R.F. Cook, High resolution surface morphology measurements using EBSD cross-correlation techniques and AFM, Ultramicroscopy 111 (2011) 1206–1213.
[5] G. Miyamoto, A. Shibata, T. Maki, T. Furuhara, Precise measurement of strain accommodation in austenite matrix surrounding martensite in ferrous alloys by electron backscatter diffraction analysis, Acta Mater. 57 (2009) 1120–1131.
[6] Y. Koizumi, S. Suzuki, K. Yamanaka, B.S. Lee, K. Sato, Y.P. Li, et al., Strain-induced martensitic transformation near twin boundaries in a biomedical Co–Cr–Mo alloy with negative stacking fault energy, Acta Mater. 61 (2013) 1648–1661.
[7] K. Yamanaka, M. Mori, Y. Koizumi, A. Chiba, Local strain evolution due to athermal gamma→epsilon martensitic transformation in biomedical Co–Cr–Mo alloys, J. Mech. Behav. Biomed. Mater. 32 (2014) 52–61.
[8] Y. Guo, T.B. Britton, A.J. Wilkinson, Slip band–grain boundary interactions in commercial-purity titanium, Acta Mater. 76 (2014) 1–12.
[9] T.B. Britton, A.J. Wilkinson, Stress fields and geometrically necessary dislocation density distributions near the head of a blocked slip band, Acta Mater. 60 (2012) 5773–5782.
[10] T.B. Britton, H. Liang, F.P.E. Dunne, A.J. Wilkinson, The effect of crystal orientation on the indentation response of commercially pure titanium: experiments and simulations, Proc. R. Soc. A—Math. Phys. Eng. Sci. 466 (2010) 695–719.
[11] A.J. Wilkinson, D. Randman, Determination of elastic strain fields and geometrically necessary dislocation distributions near nanoindents using electron back scatter diffraction, Philos. Mag. 90 (2010) 1159–1177.
[12] M.D. Vaudin, Y.B. Gerbig, S.J. Stranick, R.F. Cook, Comparison of nanoscale measurements of strain and stress using electron back scattered diffraction and confocal Raman microscopy, Appl. Phys. Lett. 93 (10 2008).
[13] P.S. Karamched, A.J. Wilkinson, High resolution electron back-scatter diffraction analysis of thermally and mechanically induced strains near carbide inclusions in a superalloy, Acta Mater. 59 (2011) 263–272.
[14] T. Zhang, D.M. Collins, F.P.E. Dunne, B.A. Shollock, Crystal plasticity and high-resolution electron backscatter diffraction analysis of full-field polycrystal Ni superalloy strains and rotations under thermal loading, Acta Mater. 80 (2014) 25–38.
[15] J. Jiang, T.B. Britton, A.J. Wilkinson, Evolution of dislocation density distributions in copper during tensile deformation, Acta Mater. 61 (2013) 7227–7239.
[16] Y. Tomota, S. Daikuhara, S. Nagayama, M. Sugawara, N. Ozawa, Y. Adachi, et al., Stress corrosion cracking behavior at inconel and low alloy steel weld interfaces, Metall. Mater. Trans. A—Phys. Metall. Mater. Sci. 45A (2014) 6103–6117.
[17] M. Ojima, Y. Adachi, S. Suzuki, Y. Tomota, Stress partitioning behavior in an fcc alloy evaluated by the in situ/ex situ EBSD-Wilkinson method, Acta Mater. 59 (2011) 4177–4185.
[18] X. Maeder, W.M. Mook, C. Niederberger, J. Michler, Quantitative stress/strain mapping during micropillar compression, Philos. Mag. 91 (2011) 1097–1107.
[19] M. Tomita, M. Nagasaka, D. Kosemura, K. Usuda, T. Tezuka, A. Ogura, Tensor evaluation of anisotropic stress relaxation in mesa-shaped SiGe layer on Si substrate by electron back-scattering pattern measurement: comparison between Raman measurement and finite element method simulation, Jpn. J. Appl. Phys. 52 (2013).
[20] S. Villert, C. Maurice, C. Wyon, R. Fortunier, Accuracy assessment of elastic strain measurement by EBSD, J. Microsc. 233 (2009) 290–301.
[21] M. Tomita, D. Kosemura, M. Takei, K. Nagata, H. Akamatsu, A. Ogura, Evaluation of strained-silicon by electron backscattering pattern measurement: comparison study with UV-Raman measurement and edge force model calculation, Jpn. J. Appl. Phys. 50 (2011).
[22] T. Ishido, H. Matsuo, T. Katayama, T. Ueda, K. Inoue, D. Ueda, Depth profiles of strain in AlGaN/GaN heterostructures grown on Si characterized by electron backscatter diffraction technique, Ieice Electron. Express 4 (2007) 775–781.
[23] S.C. Speller, T.B. Britton, G. Hughes, S. Lozano-Perez, A.T. Boothroyd, E. Pomjakushina, et al., Analysis of local chemical and structural inhomogeneities in $FeySe_{1-x}Te_x$ single crystals, Appl. Phys. Lett. 99 (2011).
[24] M. Nacke, M. Allardt, P. Chekhonin, E. Hieckmann, W. Skrotzki, J. Weber, Investigations on residual strains and the cathodoluminescence and electron beam induced current signal of grain boundaries in silicon, J. Appl. Phys. 115 (2014).
[25] J.A. Howell, M.D. Vaudin, R.F. Cook, Orientation, stress, and strain in an (001) barium titanate single crystal with 90A degrees lamellar domains determined using electron backscatter diffraction, J. Mater. Sci. 49 (2014) 2213–2224.
[26] T.B. Britton, J. Jiang, R. Clough, E. Tarleton, A.I. Kirkland, A.J. Wilkinson, Assessing the precision of strain measurements using electron backscatter diffraction-part 1: Detector assessment, Ultramicroscopy 135 (2013) 126–135.
[27] T.B. Britton, J. Jiang, R. Clough, E. Tarleton, A.I. Kirkland, A.J. Wilkinson, Assessing the precision of strain measurements using electron backscatter diffraction-Part 2: Experimental demonstration, Ultramicroscopy 135 (2013) 136–141.
[28] S.R. Niezgoda, R.J. McCabe, C.N. Tomé, Quantification of strain and orientation measurement error in cross-correlation EBSD in hexagonal close-packed materials, Scr. Mater. 67 (2012) 818–821.
[29] J. Jiang, T.B. Britton, A.J. Wilkinson, Accumulation of geometrically necessary dislocations near grain boundaries in deformed copper,", Philos. Mag. Lett. vol. 92 (2012) 580–588.
[30] D. Chen, J.-C. Kuo, W.-T. Wu, Effect of microscopic parameters on EBSD spatial resolution, Ultramicroscopy 111 (2011) 1488–1494.

[31] C. Sorensen, J.A. Basinger, M.M. Nowell, D.T. Fullwood, Five-parameter grain boundary inclination recovery with ebsd and interaction volume models, Metall. Mater. Trans. A 45 (2014) 4165–4172.
[32] S.I. Wright, M.M. Nowell, R. de Kloe, L.S. Chan, Orientation precision of electron backscatter diffraction measurements near grain boundaries, Microsc. Microanal. 20 (2014) 852–863.
[33] T.B. Britton, A.J. Wilkinson, Measurement of residual elastic strain and lattice rotations with high resolution electron backscatter diffraction, Ultramicroscopy 111 (2011) 1395–1404.
[34] S. Zaefferer, On the formation mechanisms, spatial resolution and intensity of backscatter Kikuchi patterns, Ultramicroscopy 107 (2007) 254–266.
[35] F. Humphreys, Review grain and subgrain characterisation by electron backscatter diffraction, J. Mater. Sci. 6 (2001) 3833–3854.
[36] J. Jiang, T. Ben Britton, A.J. Wilkinson, Accumulation of geometrically necessary dislocations near grain boundaries in deformed copper, Philos. Mag. Lett. 92 (2012) 580–588.
[37] P.D. Littlewood, T.B. Britton, A.J. Wilkinson, Geometrically necessary dislocation density distributions in Ti–6Al–4V deformed in tension, Acta Mater. 59 (2011) 6489–6500.
[38] J. Jiang, T.B. Britton, A.J. Wilkinson, Mapping type III intragranular residual stress distributions in deformed copper polycrystals, Acta Mater. 61 (2013) 5895–5904.